Rankin, AJ., Krauskopf, B., Lowenberg, MH., & Coetzee, E. B. (2009). Operational Parameter Study of Aircraft Dynamics on the Ground. *Journal of Computational and Nonlinear Dynamics*, *5*(2), -. [021007]. https://doi.org/10.1115/1.4000797

Operational Parameter Study of Aircraft Dynamics on the Ground

James Rankin*, Bernd Krauskopf, Mark Lowenberg,
Faculty of Engineering, University of Bristol, Bristol, UK, BS8 1TR
and Etienne Coetzee,
Landing Gear Systems, Airbus, Bristol, UK, BS99 7AR

Abstract

The dynamics of passenger aircraft on the ground are influenced by the nonlinear characteristics of several components, including geometric nonlinearities, the aerodynamics and interactions at the tyre-ground interface. We present a fully parametrised mathematical model of a typical passenger aircraft that includes all relevant nonlinear effects. The full equations of motion are derived from first principles in terms of forces and moments acting on a rigid airframe, and they include implementations of the local models of individual components. The overall model has been developed from and validated against an existing industry-tested SimMechanics model.

The key advantage of the mathematical model is that it allows for comprehensive studies of solutions and their stability with methods from dynamical systems theory, in particular, the powerful tool of numerical continuation. As a concrete example, we present a bifurcation study of how fixed-radius turning solutions depend on the aircraft's steering angle and centre of gravity position. These results are represented in a compact form as surfaces of solutions, on which we identify regions of stable turning and regions of laterally unstable solutions. The boundaries between these regions are computed directly and they allow us to determine ranges of parameter values for safe operation. The robustness of these results under the variation of additional parameters, specifically, the engine thrust and aircraft mass, are investigated. Qualitative changes in the structure of the solutions are identified and explained in detail. Overall our results give a complete description of the possible turning dynamics of the aircraft in dependence on four parameters of operational relevance.

1 Introduction

There are two primary concerns for commercial aircraft during taxiing: the safety of passengers and the economy of operations. Methods used to control an aircraft and the conditions under which it operates directly affect its dynamics on the ground. The design of automated

*Corresponding author: Address: Department of Engineering Mathematics, Faculty of Engineering, University of Bristol, Bristol, BS8 1TR, UK; phone: +44 (0) 1173317409; e-mail:j.rankin@bris.ac.uk

control systems that can take these considerations into account is the ultimate goal in the study of aircraft ground dynamics. Computer simulations of advanced multi-body models play an important role in both the design stages of new aircraft and the study of existing aircraft. Once a model has been developed and validated, it is relatively inexpensive, compared to actual ground taxi tests, to simulate the model numerically so that many simulation runs can be performed. Specifically, computer simulations have been used in conjunction with actual tests in the study of aircraft ground manoeuvres [1, 2]. An important aspect of any aircraft model are nonlinearities that are introduced via geometry and specific properties of components, such as the steering mechanism, the tyres and aerodynamic surfaces. Since nonlinearities are known to play an important role in the dynamics of a given system, it is important to fully incorporate them as part of the model and the analysis. A number of nonlinear models have been developed and investigated in the fields of aircraft dynamics, mostly with more traditional methods, to study the dynamics of aircraft in flight [3] and on the ground [4].

In this paper we employ the mathematical tool of numerical bifurcation analysis, which allows one to find solutions of a nonlinear system, follow them in parameters and determine their stability in an efficient way; one also speaks of numerical continuation. This approach is implemented in software packages such as AUTO [5], which have been used to great effect for the analysis of nonlinear systems in many areas of applications; see, for example, [6] as an entry point to the literature. Continuation techniques are also beginning to make an impact in areas that are of relevance to aircraft ground dynamics, for example, in the study of automotive vehicles [7] and the flight dynamics of aircraft [8, 9]. A previous bifurcation study of aircraft ground dynamics by the authors in Reference [10] was based on an industry-tested software model, developed in the multibody systems software package SimMechanics [11, 12], which was successfully coupled to the package AUTO. This allowed for a comprehensive account of the possible turning dynamics of the aircraft for a particular aircraft configuration, where the steering angle acted as the main parameter. The difficulty with such a software model lies in its black-box nature. In particular, not all operationally relevant parameters are accessible for bifurcation studies, and we also encountered some numerical difficulties in computing periodic solutions.

The purpose of this paper is to develop a fully parametrised mathematical model of an aircraft as a vehicle on the ground, and to demonstrate that it allows us to extend previous work with a bifurcation study into the effect of several operational parameters. The new mathematical model takes the form of a system of coupled ordinary differential equations (ODEs) that is derived by equating forces and moments. Specifically, we consider a tricycle model of a typical mid-sized single aisle passenger aircraft in which the nose gear is used for steering. The airframe is considered as a rigid body with six degrees of freedom and the equations of motion are derived by balancing the respective forces and moments. Specific sub-components are modelled in accordance with industry experience and test data, and nonlinear effects are included in the models of the tyres and the aerodynamics. In this way, the overall mathematical model incorporates a sufficient and relevant level of complexity, in particular, the nonlinearities inherent in various components. This new model provides several advantages over the existing model, especially when used with continuation software. Its general functionality and computational efficiency with the software package AUTO is dramatically improved. Furthermore, the model does not suffer from a black-box nature,

which means that all variables and parameters — both design parameters (such as dimensions of the aircraft) and operational parameters (such as total mass and center of gravity position) — are fully accessible.

During ground manoeuvres aircraft make turns by adjusting the steering angle of the nose gear, generally, for a fixed thrust level of the engines. The specific aircraft ground manoeuvre that we consider here is a fixed steering angle turn, where we assume that neither accelerations nor braking through the tyres are applied. The performance of turning circle manoeuvres is a standard test case for aircraft; in our model when the aircraft follows a turning circle (of fixed radius) this corresponds to a steady state solution of the system (in the body-axes). It is these turning circle solutions and their stability that are the main subject of our bifurcation analysis. With the use of the continuation package AUTO turning solutions can be tracked or continued under the variation of parameters. Furthermore, changes in stability can be detected. They occur at special points, called bifurcations [13], and result in a qualitative change in the dynamics of the system. Turning solutions and their bifurcations can thus be represented by plotting a system state as a function of one or more parameters.

The development of the mathematical model was guided by the existing multibody model in SimMechanics, and the first step was the validation of the model via a direct comparison with existing results from Reference [10]. This validation is demonstrated here with a one-parameter bifurcation analysis that focuses in detail on the agreement between the different types of solutions in each model. In particular, we identify different types of stable turns and also laterally unstable turning solutions for which the aircraft loses lateral stability. The different solutions are presented across the full range of the steering angle for a particular aircraft setup, which allows for a comprehensive comparison between the models.

We then present an extensive bifurcation analysis of turning solutions of the aircraft in dependence on several operational parameters. One-parameter continuation runs are computed in the steering angle at many discrete points of centre of gravity positions (over a suitable range). Two-parameter continuation is used to follow curves of bifurcation points directly to determine regions where turning is unstable. The results are represented as surfaces of solutions that describe the possible dynamics over the full range of the two parameters, the steering angle and the centre of gravity position. We find that a curve of limit point bifurcations forms a fold in the surface of solutions; crossing this curve in parameter space results in a significant change in the radius of the turning circle that the aircraft attempts to follow. Additionally, we find that a curve of Hopf bifurcations bounds a region of unstable turning solutions for which the aircraft follows a laterally unstable motion relative to the unstable turning solution. The robustness of these results is further investigated under the variation of the aircraft mass and the thrust level. We find that quite small changes in thrust result in a sequence of qualitative changes of the solution surface. This occurs for two different mass cases (heavy and light aircraft) but at different thrust levels. Overall, a heavier aircraft will make stable turns over a larger range of centre of gravity positions and at higher thrust levels. We also find that the region of laterally unstable behaviour grows more rapidly with increased thrust for a lighter aircraft.

The paper is organised as follows: In Section 2 full details of the new model are given. Its validation against the existing SimMechanics model is demonstrated in Section 3. An extensive bifurcation analysis in several parameters is the subject of Section 4. Finally,

conclusions and directions of future work are presented in Section 5.

2 Mathematical Model

In this section we give details of the derivation and implementation of a fully parametrised mathematical model of a typical mid-sized single aisle passenger aircraft. Our model is effectively a fully parametrised mathematical version of an industry-tested SimMechanics [12] model that was used in a previous study [10]. Motivations for its development are: to overcome the black-box nature of a model written in SimMechanics (especially concerning full access to relevant system parameters), to improve functionality with the continuation package AUTO [5], and to increase the computational efficiency so that more elaborate bifurcation studies become feasible. The mathematical model has been derived via force and momentum equations, coupled to relevant subsystem descriptions. It has been fully validated against the existing SimMechanics model; see Section 3.

The aircraft modeled here has a tricycle configuration in which the nose gear is used for steering. We model the aircraft as a single rigid body with six degrees of freedom (DOF); three translational DOF and three rotational DOF. On the aircraft there are two tyres per gear. Due to the small separation distance they can be assumed to act in unison and, hence, are described as a single tyre in the model. We do not include oleos in the model presented here, that is, we assume the landing gears to be rigid. The reason for this simplifying assumption is that oleo dynamics are not excited in turning as considered in the bifurcation study in Section 4. However, oleos could be included into the model, but at the expense of increasing its dimensionality.

Throughout this study we use one of the conventionally accepted coordinate systems for aircraft. Specifically, the positive x-axis points towards the nose of the aircraft, the z-axis is toward the ground and the y-axis completes the right-handed coordinate system. This body coordinate system is assumed to coincide with the aircraft's principal axes of inertia, a reasonable assumption due to symmetries of the airframe. The equations of motion were derived from Newton's Second Law by balancing either the forces or moments in each degree of freedom [14].

In Figure 1 the relative positions and directions of the force elements that act on the aircraft are shown in the three standard projections. These diagrams illustrate how the equations of motion are derived by balancing force elements along each axis and moment elements about each axis. The equations of motion for the velocities in the body coordinate system of the aircraft are given as six ordinary differential equations (ODEs):

$$\begin{aligned}
m(\dot{V}_x + V_z W_y - V_y W_z) = {} & F_{xTL} + F_{xTR} - F_{xR} - F_{xL} - F_{xN}\cos(\delta) - \\
& F_{yN}\sin(\delta) - F_{xA} + F_{zW}\sin(\theta), && (1)\\
m(\dot{V}_y + V_x W_z - V_z W_x) = {} & F_{yR} + F_{yL} + F_{yN}\cos(\delta) - F_{xN}\sin(\delta) + F_{yA}, && (2)\\
m(\dot{V}_z + V_y W_x - V_x W_y) = {} & F_{zW} - F_{zR} - F_{zL} - F_{zN} - F_{zA}, && (3)\\
I_{xx}\dot{W}_x - (I_{yy} - I_{zz}) W_y W_z = {} & l_{yL}F_{zL} - l_{yR}F_{zR} - l_{zL}F_{yL} - l_{zR}F_{yR} - \\
& l_{zN}F_{yN}\cos(\delta) + l_{zN}F_{xN}\sin(\delta) + l_{zA}F_{yA} + M_{xA}, && (4)
\end{aligned}$$

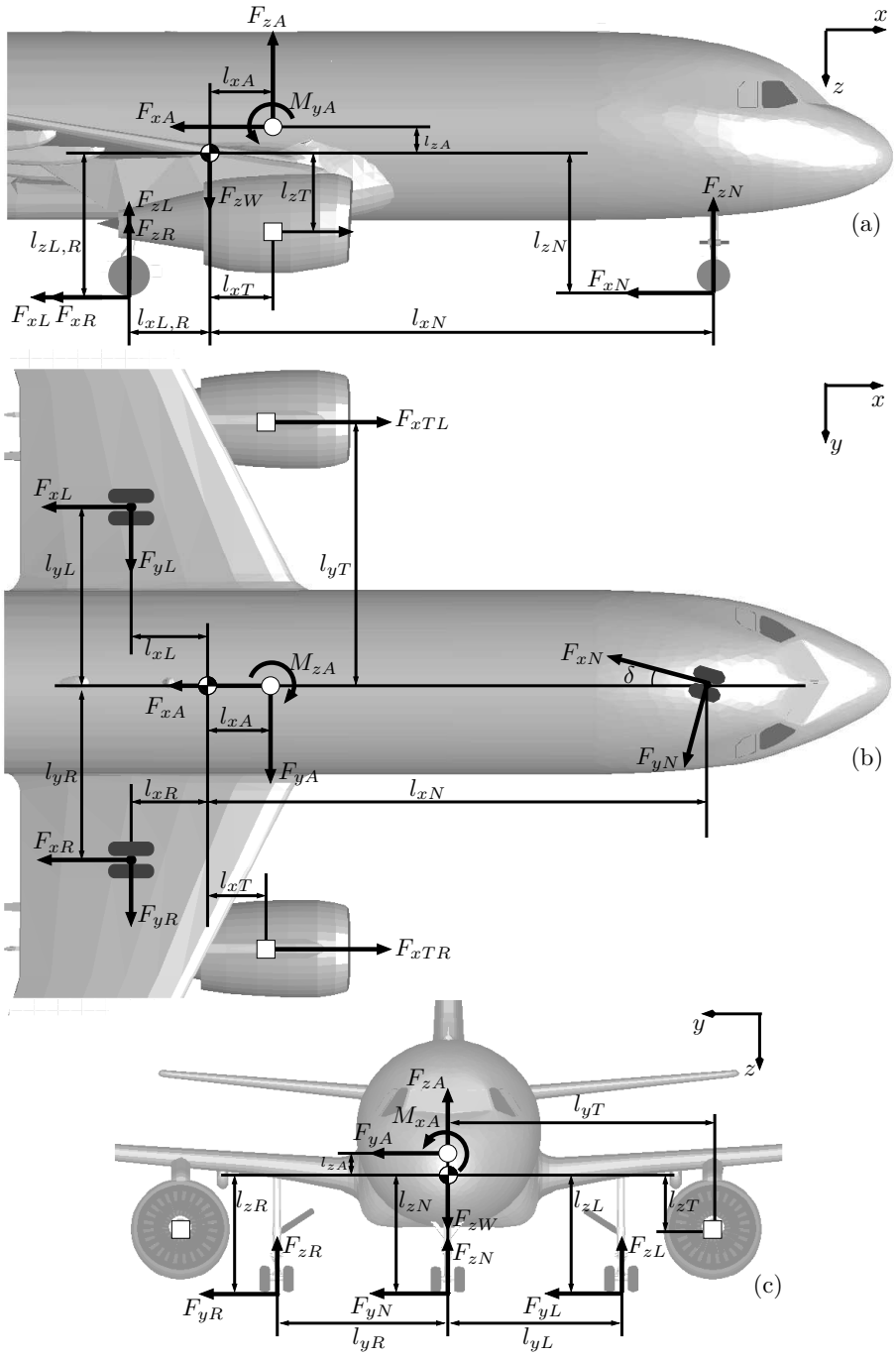

Figure 1: Schematic diagram showing relative positions of force elements F_* acting on the airframe with dimensions defined by l_* in Table 1. Three projections are shown in the aircraft's body coordinate system: the (x, z)-plane in panel (a), the (x, y)-plane in panel (b), and the (y, z)-plane in panel (c). The centre of gravity position is represented by a checkered circle, the aerodynamic centre by a white circle and the thrust centre of each engine by a white square.

$$I_{yy}\dot{W}_y - (I_{zz} - I_{xx})W_xW_z = l_{xN}F_{zN} - l_{zN}F_{xN}\cos(\delta) - l_{zN}F_{yN}\sin(\delta) - l_{xR}F_{zR} - l_{zR}F_{xR} - l_{xL}F_{zL} - l_{zL}F_{xL} + l_{zT}F_{xTL} + l_{zT}F_{xTR} + l_{zA}F_{xA} + l_{xA}F_{zA} + M_{yA}, \quad (5)$$

$$I_{zz}\dot{W}_z - (I_{xx} - I_{yy})W_xW_y = l_{yR}F_{xR} - l_{yR}F_{xL} - l_{xR}F_{yR} - l_{xL}F_{yL} + l_{xN}F_{yN}\cos(\delta) - l_{xN}F_{xN}\sin(\delta) + l_{xA}F_{yA} + l_{yT}F_{xTL} - l_{yT}F_{xTR} + M_{zA}. \quad (6)$$

Here a dot notation is used to show the first derivative with respect to time of these states. The dimensions l_*, given in Table 1, are defined in terms of the centre of gravity position which is parametrized as CG. The parameter CG is defined as a percentage measured along the mean aerodynamic chord l_{mac}, taken from the leading edge. The aircraft mass m as defined for two cases presented in the bifurcation analysis are given in Table 1; corresponding values of the principal moments of inertia I_{xx}, I_{yy} and I_{zz} are used in the model. The velocities along each of the aircraft's axes are given by V_* and the rotational velocities about the axes by W_*. The weight of the aircraft acting at the centre of gravity (CG) position is denoted $F_{zW} = mg$ and is assumed to act along the z-axis in the aircraft body coordinate system because the pitch and roll angles remain relatively small throughout this analysis. The steering angle applied to the nose gear, defined in degrees, is denoted δ. It is used as a parameter in the bifurcation analysis. The modeling of tyre forces is discussed in Section 2.1 and the orthogonal force elements on each of the nose, main right and main left tyres are denoted F_{*N}, F_{*R} and F_{*L}, respectively. The modeling of the aerodynamics is discussed in Section 2.2. The individual aerodynamic force and moment elements are defined with respect to the aerodynamic centre of the aircraft and are denoted F_{*A} and M_{*A}, respectively. The thrust force is assumed to act parallel to the x-axis of the aircraft and is denoted F_{xT}; the total thrust force from both of the engines is parametrized as T which is defined as a percentage of the maximum available thrust.

The states that vary most significantly during the aircraft's motion are the velocity V_x in the x-direction, the velocity V_y in the y-direction, and the angular velocity W_z about the z-axis (yaw velocity); they are calculated from equations (1), (2) and (6), respectively. A reasonable approximation of the aircraft's dynamics is given by these three equations alone. However, to calculate the asymmetric loading on the landing gears dynamically and with a high level of accuracy it is necessary to solve the equations in the other degrees of freedom: the vertical velocity V_z, angular velocity W_x about the x-axis (roll velocity) and angular velocity W_y about the y-axis (pitch velocity) given by equations (3), (4) and (5), respectively.

To calculate the position of the aircraft as it moves over the ground plane it is necessary to do so with reference to a fixed location and orientation in space. Therefore, we solve a set of equations describing the position of the aircraft in the world coordinate system with position (X, Y, Z) and angular orientation given by the Euler angles (ψ, θ, ϕ), where ψ is the yaw angle, θ the pitch angle and ϕ the roll angle. The plane given by $Z = 0$ is the (flat) ground plane. Transformations between the body coordinate system and the world coordinate system can be performed by applying the standard sequence of rotations given in Reference [15]. Defining the velocities in the world axis as V_{xW}, V_{yW} and V_{zW}, the velocity

transformation equations are given by:

$$\begin{pmatrix} V_{xW} \\ V_{yW} \\ V_{zW} \end{pmatrix} = \begin{bmatrix} C_\theta C_\psi & S_\phi S_\theta C_\psi - C_\phi S_\psi & C_\phi S_\theta C_\psi + S_\phi S_\psi \\ C_\theta S_\psi & S_\phi S_\theta S_\psi - C_\phi C_\psi & C_\phi S_\theta S_\psi + S_\phi C_\psi \\ -S_\theta & S_\phi C_\theta & C_\phi C_\theta \end{bmatrix} \begin{pmatrix} V_x \\ V_y \\ V_z \end{pmatrix}, \tag{7}$$

where $C_* = \cos(*)$ and $S_* = \sin(*)$ for notational convenience. Defining the angular velocities in the world axis as W_{xW}, W_{yW} and W_{zW}, the angular velocity transformation equations are given by:

$$\begin{pmatrix} W_{xW} \\ W_{yW} \\ W_{zW} \end{pmatrix} = \begin{bmatrix} 1 & S_\phi S_\theta / C_\theta & C_\phi S_\theta / C_\theta \\ 0 & C_\phi & -S_\phi \\ 0 & S_\phi / C_\theta & C_\phi / C_\theta \end{bmatrix} \begin{pmatrix} W_x \\ W_y \\ W_z \end{pmatrix}. \tag{8}$$

Therefore the equations for the position of the aircraft are given by:

$$\begin{aligned} \dot{X} &= V_{xW}, \quad \dot{\psi} = W_{zW}, \\ \dot{Y} &= V_{yW}, \quad \dot{\theta} = W_{yW}, \\ \dot{Z} &= V_{zW}, \quad \dot{\phi} = W_{xW}. \end{aligned} \tag{9}$$

The position (X, Y) and orientation ψ are used to plot trajectories of the aircraft motion. The height Z above the ground plane and the angles θ and ϕ that the aircraft makes with the ground plane are used to calculate the load distribution between landing gears.

2.1 Tyre modeling

The force elements acting on the tyres are calculated with a tyre model developed by a GARTEUR action group investigating ground dynamics [16], it was also used in the SimMechanics model [10]. The main difference now is that the local velocities and displacements of the tyres at the ground interfaces are calculated using equations in terms of the aircraft states instead of being given by SimMechanics. The model used here assumes that the roll axis of the tyre is always parallel to the ground because the pitch and yaw angles of the aircraft remain relatively small. It is therefore appropriate to use the velocities of the aircraft in the body coordinate system and Euler angles to calculate local displacements and velocities of the tyres. This section focuses on these calculations, which are used in obtaining the tyre forces.

To model the vertical force component on the tyre a linear spring and damper system can be used [11, chapter 4]. For example, the total force acting on the nose gear is:

$$F_{zN} = -k_{zN}\delta_{zN} - c_{zN}V_{zN} \tag{10}$$

where V_{zN} is the vertical velocity of the nose gear tyre, and δ_{zN} is the nose gear tyre deflection representing the change in tyre diameter between the loaded and unloaded condition. The stiffness coefficients k_z* and damping coefficient c_{z*} are specified in Table 1. Differences in the vertical velocity and deflection of each tyre give the asymmetric load distribution between the gears. The vertical velocity of each tyre can be calculated in terms of the velocities in the body coordinate system as:

$$\begin{aligned} V_{zN} &= V_z - l_{xN}W_y, \\ V_{zR} &= V_z + l_{yR}W_x + l_{xR}W_y, \\ V_{zL} &= V_z - l_{yL}W_x + l_{xL}W_y, \end{aligned} \tag{11}$$

Symbol	Parameter	Value	
	dimensions relative to CG-position		
l_{xN}	x-distance to nose gear	$(10.186 + CG \div 100 \times l_{mac})$ m	
l_{zN}	z-distance to nose gear	2.932 m	
$l_{xR,L}$	x-distance to main gears	$(2.498 - CG \div 100 \times l_{mac})$m	
$l_{yR,L}$	y-distance to nose gear	3.795 m	
$l_{zR,L}$	z-distance to nose gear	2.932 m	
l_{xA}	x-distance to aerodynamic centre	$([0.25 - CG \div 100] \times l_{mac})$m	
l_{zA}	z-distance to aerodynamic centre	0.988 m	
l_{xT}	x-distance to thrust centre	$([0.25 - CG \div 100] \times l_{mac})$m	
$l_{yTR,TL}$	y-distance to thrust centre	5.755 m	
l_{zT}	z-distance to thrust centre	1.229 m	
	mass	light case	heavy case
m	mass of the aircraft	45420 kg	75900 kg
	tyre parameters		
k_{zN}	stiffness coeff. of nose tyre	1190 kN/m	
k_{zM}	stiffness coeff. of main tyre	2777 kN/m	
c_{zN}	damping coeff. of nose tyre	1000 Ns/m	
c_{zM}	damping coeff. of main tyre	2886 Ns/m	
μ_R	rolling resistance coeff.	0.02	
	aerodynamics parameters		
l_{mac}	mean aerodynamic chord	4.194 m	
S_w	wing surface area	122.4 m^2	
ρ	density of air	1.225 kg/m^3	

Table 1: System parameters and their values as used in the model.

where V_{z*} is the local vertical velocity of the respective tyre. Due to the assumptions that the roll axes of the tyres remain parallel to the ground and that the pitch and roll angles of the aircraft remain small, the deflection of each tyre is given in terms of the aircraft's position states in the world coordinate system as:

$$\begin{aligned} \delta_{zN} &= -l_{zN} - Z + l_{xN}\theta, \\ \delta_{zR} &= -l_{zR} - Z - l_{xR}\theta - l_{yR}\phi, \\ \delta_{zL} &= -l_{zL} - Z - l_{xL}\theta + l_{yL}\phi. \end{aligned} \tag{12}$$

The longitudinal and lateral forces at the tyre-ground interface depend on the vertical load acting on the tyre and on its slip angle. The slip angle of a tyre is the angle the tyre makes with its direction of motion. For each respective tyre, the slip angle α_* is defined in terms of its local longitudinal velocity V_{x*} and its local lateral velocity V_{y*} as:

$$\alpha_* = \arctan\left(\frac{V_{y*}}{V_{x*}}\right). \tag{13}$$

Therefore, to find the slip angle it is necessary to find the longitudinal and lateral velocity of each tyre. These velocities are calculated in terms of the aircraft's velocities in the body coordinate system and the steering angle applied to the nose gear δ as:

$$\begin{aligned} V_{xN} &= V_x\cos(\delta) + (V_y + l_{xN}W_z)\sin(\delta), \\ V_{yN} &= (V_y + l_{xN}W_z)\cos(\delta) - V_x\sin(\delta), \\ V_{xR} &= V_x - l_{yR}W_z, \\ V_{yR} &= V_y - l_{xR}W_z, \\ V_{xL} &= V_x + l_{yL}W_z, \\ V_{yL} &= V_y - l_{xL}W_z. \end{aligned} \tag{14}$$

Longitudinal forces on the tyres are due to the rolling resistance force caused by hysteresis in the rubber of the tyre. The pressure in the leading half of the contact patch is higher than in the trailing half, and consequently the resultant vertical force does not act through the middle of the wheel. A horizontal force in the opposite direction of the wheel movement is needed to maintain an equilibrium. This horizontal force is known as the rolling resistance [17, pp. 8-18]. The ratio of the rolling resistance F_x, to vertical load F_z, on the tyre is known as the coefficient of rolling resistance μ_R as given in Table 1 [18]. Therefore, the rolling resistance force on the respective tyre F_{x*} is given by

$$F_{x*} = -\mu_R F_{z*}\cos(\alpha_*), \tag{15}$$

which incorporates a cosine function to capture two key features. Firstly, the longitudinal force drops off to zero when the tyre is moving sideways ($\alpha_* = \pm 90°$) and secondly, there is a sign change when the direction of motion changes ($|\alpha_*| > 90°$).

When no lateral force is applied to a tyre, the wheel moves in the same direction as the wheel plane. When a side force is applied, the tyre generates a slip angle α_* as defined in Equation (13). For small slip angles ($\alpha_* < 5°$) the tyre force increases linearly after which

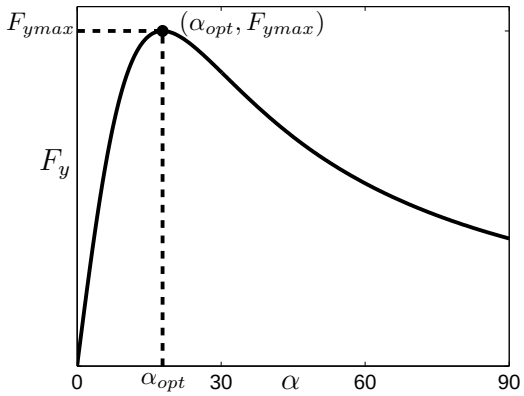

Figure 2: Lateral force F_y plotted against slip angle α as calculated from Equation (16). The maximum point F_{ymax} that can be generated by the tyre occurs at the 'optimal' slip angle α_{opt}.

there is a nonlinear relationship [17, pp. 30-38]. The lateral force on the respective tyre F_{y*} is a function of α_* and can be represented as:

$$F_{y*}(\alpha_*) = 2\frac{F_{ymax*}\alpha_{opt*}\alpha_*}{\alpha_{opt*}^2 + \alpha_*^2}, \tag{16}$$

where F_{ymax*} is the maximum force that the tyre can generate and α_{opt*} is the 'optimal' slip angle at which this occurs. The parameters F_{ymax*} and α_{opt*} depend quadratically on the vertical force on the tyre F_{z*} and, hence, change dynamically in the model. The values for nose gear tyres F_{ymaxN} and α_{optN}, and main gear tyres $F_{ymaxR,L}$ and $\alpha_{optR,L}$ are obtained from the equations:

$$\begin{aligned}
F_{ymaxN} &= -3.53 \times 10^{-6} F_{zN}^2 + 8.83 \times 10^{-1} F_{zN}, \\
\alpha_{optN} &= 3.52 \times 10^{-9} F_{zN}^2 + 2.80 \times 10^{-5} F_{zN} + 13.8, \\
F_{ymaxR,L} &= -7.39 \times 10^{-7} F_{zR,L}^2 + 5.11 \times 10^{-1} F_{zR,L}, \\
\alpha_{optR,L} &= 1.34 \times 10^{-10} F_{zR,L}^2 + 1.06 \times 10^{-5} F_{zR,L} + 6.72.
\end{aligned} \tag{17}$$

For values of α_* outside the quadrant of $\alpha_* \in (0°, 90°)$, the curve in Figure 2 is reflected appropriately to either represent the tyre rolling backwards or turning in the opposite direction. Details of extending Equation (16) in this way are given in Reference [10].

2.2 Modeling the aerodynamics

Aerodynamic effects are nonlinear because the forces are proportional to the square of the velocity of the aircraft. Due to the geometry of the aircraft, the forces also depend nonlinearly on the angle the it makes with the airflow, the sideslip angle β and on the angle of attack σ. We consider ground manoeuvres, with no incident wind. Hence, the sideslip angle β of the entire aircraft is equal to and interchangeable with its slip angle. The slip angle of the aircraft is defined in the same way as the tyres, but this time in terms of the velocities of the entire aircraft: $\alpha_{ac} = \arctan(V_y/V_x)$. Because we are studying ground manoeuvres the angle

of attack σ remains relatively steady. There are six components to the aerodynamic forces; three translational and three moments. The forces are assumed to act at the aerodynamic centre of the aircraft [14], defined as 25% along the mean aerodynamic chord from its leading edge. The six force elements are given by

$$\begin{array}{ll} F_{xA} = \frac{1}{2}\rho|V|^2 S_w C_x(\alpha_{ac},\sigma), & M_{xA} = \frac{1}{2}\rho|V|^2 S_w l_{mac} C_l(\alpha_{ac},\sigma), \\ F_{yA} = \frac{1}{2}\rho|V|^2 S_w C_y(\alpha_{ac},\sigma), & M_{yA} = \frac{1}{2}\rho|V|^2 S_w l_{mac} C_m(\alpha_{ac},\sigma), \\ F_{zA} = \frac{1}{2}\rho|V|^2 S_w C_z(\alpha_{ac},\sigma), & M_{zA} = \frac{1}{2}\rho|V|^2 S_w l_{mac} C_n(\alpha_{ac},\sigma), \end{array} \tag{18}$$

where the parameters ρ, S_w and l_{mac} are defined in Table 1. The dimensionless coefficient functions C_* depend nonlinearly on α_{ac} and σ and are based on wind-tunnel data and results from computational fluid dynamics. The coefficients used here were obtained from a model developed by the GARTEUR group [16].

3 Model validation

We now present results that were used as part of the validation process for the mathematical model described in Section 2 against the established SimMechanics model [10]. Specifically, we show in Figure 3 a comparison of a one-parameter bifurcation study of turning solutions as a function of the steering angle δ. Throughout Figure 3, solutions for the mathematical model (1)–(6) are in grey and those of the SimMechanics model are in black. This comparison shows that there is a high level of agreement between the two models over the entire relevant range of δ. Furthermore, a detailed comparison of periodic solutions (corresponding to unstable turning) shows that the two models also agree closely in terms of laterally unstable behaviour.

Figure 3(a) shows a direct comparison of a bifurcation diagram in δ of turning solutions for $CG = 14\%$ and $T = 19\%$, where the forward velocity of the aircraft V_x is used as a measure of the solution; the data from the SimMechanics model has been reproduced from Reference [10, Figure 4]. A single branch of solutions originates in the top left of the diagram and terminates in the top right; stable parts are solid curves and unstable parts are dashed curves. Changes in stability occur at the limit point bifurcations L_1, L_2, L_3, L_4 and at the Hopf bifurcation point H_2. There is a branch of periodic solutions that originates from H_2; the maximum and minimum velocities of these solutions are shown as a continuous solid grey curve for model (1)–(6) and as a series of black dots at discrete points for the SimMechanics model. More details of the solutions represented in the bifurcation diagram and the significance of passing the different bifurcations is discussed in greater detail in Reference [10].

Overall there is close agreement in Figure 3(a) between the bifurcation curves of the two models. Any differences are quite small and restricted to certain regions of operation. At the initial point where $\delta = 0$ the aircraft travels in a straight line. Here model (1)–(6) has a velocity of $V_x \approx 87$m/s, while the SimMechanics model has a velocity of $V_x \approx 90$m/s. This small difference exists on the branch between the initial point and the bifurcation point L_1 along which the solutions represent large radius turning circles. When the steering angle is increased to a value beyond L_1 the aircraft will attempt to follow a smaller radius turning circle at low velocity. Following the solution branch through L_1, at which there is a change

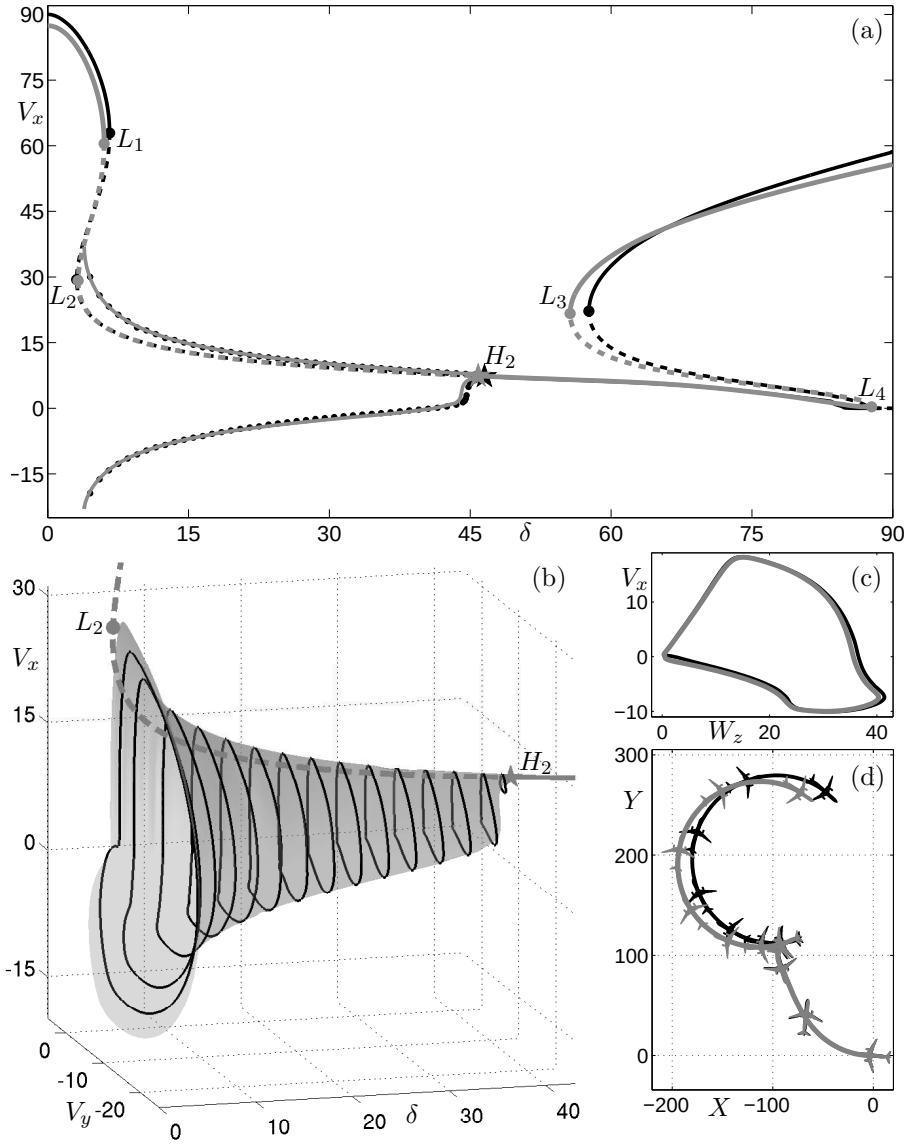

Figure 3: Comparison between the mathematical model (1)–(6) (black curves) and the SimMechanics model (grey curves). Panel (a) shows one-parameter bifurcation diagrams for varying steering angle δ and fixed $CG = 14\%$ and $T = 19\%$. There is a single branch of turning solutions; stable parts are solid and unstable parts are dashed. Changes in stability occur at the bifurcation points L_{1-4} and H_2. The maximum and minimum forward velocity of a branch of periodic solutions originating at H_2 are also shown. Panel (b) shows the branch of periodic solutions plotted in the (δ, V_y, V_x)-projection; the (grey) surface was computed from the mathematical model and the individual orbits (black closed curves) on the surface were computed with the SimMechanics model. Panel (c) shows a comparison of the individual periodic orbits at $\delta = 10°$ in the (W_z, V_x)-projection. The corresponding CG-trace of the aircraft in the (X, Y) ground plane is shown in panel (d) with markers indicating the orientation of the aircraft at regular time intervals.

in stability, we see that the curves computed with the different models agree closely. Along section of the solution branch that is approximately horizontal, which represents small radius turns, the two models remain in almost exact agreement up to the bifurcation L_4. A branch of periodic solutions originates at the Hopf bifurcation H_2 which is the typical behaviour [13]. The respective maximum and minimum velocities along the branch of periodic solutions show a high level of agreement; these solutions are discussed in further detail below. The limit point bifurcation L_4 is only detected in model (1)–(6), but nevertheless the two models exhibit qualitatively the same behaviour in this region of the bifurcation diagram. For the large radius solutions along the branch between L_3 and the final point in the top right of Figure 3(a) the two models show again a slight difference in velocity along the branch. Furthermore, the limit point bifurcation L_3 occurs at a somewhat lower value of δ in model (1)–(6).

Figure 3(b) shows the branch of periodic solutions in the (δ, V_y, V_x)-projection, where V_y is the lateral velocity of the aircraft. In a previous study these solutions were studied in great detail and four types of qualitatively different behaviour were identified [10]. We show this data to demonstrate that the two models agree to a high level of detail even in terms of the laterally unstable motion that the periodic solutions represent. The periodic solutions form a surface in parameter $\times$ phase space. For the mathematical model (1)–(6) it can be computed directly by continuation of the periodic solutions from the Hopf bifurcation point H_2. For the SimMechanics model, on the other hand, periodic solutions can only be found at discrete values of δ by numerical simulation. The two models show excellent agreement: the (black) periodic orbits of the SimMechanics model lie on the grey surface of periodic solutions of model (1)–(6) to very good accuracy. Figure 3(c) shows a specific periodic orbit in more detail for $\delta = 10^\circ$ in the (V_x, W_z)-projection; W_z is the angular velocity in degrees of the aircraft about its vertical axis. The two periodic orbits indeed agree so closely that the (black) periodic orbit of the SimMechanics model is eclipsed by that of model (1)–(6). Figure 3(d) shows a trace of the aircraft's centre of gravity position over one period of the its motion in the (X, Y) ground plane for each of the two models. Markers drawn to scale on the CG-trace show the aircraft's relative direction of motion at equal time intervals along the trajectory. The trajectories computed with the two models agree very closely in the initial section but appear to diverge slightly after a point close to $(X, Y) = (100, 100)$ where the tangent of the CG-trace changes very quickly. In fact, at this point in the trajectory, where the velocity of the aircraft is very low, the plot exaggerates a very small discrepancy in the amount the aircraft rotates. Either side of this point the trajectories agree very precisely.

In summary of the validation process, the models agree very closely both in terms of the turning circle solutions represented in the bifurcation diagram, as well as the lateral unstable periodic solutions. The agreement is well within the accuracy of comparisons with actual test data, so that the mathematical model (1)–(6) can be used with confidence. In the bifurcation diagram there were only some small observable differences at high velocities. These differences occur because the mathematical model (1)–(6) does not include the oleos. As we checked, with the oleos included the aircraft assumes a slightly elevated angle of attack that increases the lift and, therefore, reduces the loads on the tyres. This, in turn, reduces the longitudinal and lateral forces on the tyres and, thus, the aircraft travels faster with the oleos included. The slight discrepancy in the amount the aircraft rotates at the point of lowest velocity of the periodic solution is also due to the fact that the oleos are

not included in model (1)–(6). Namely, with oleos a slight shift of weight from the inner to the outer gears accounts for a greater rotation as exhibited by the SimMechanics model in Figure 3(d). In spite of these small discrepancies, the dynamics of the two models are still sufficiently close and qualitatively the same over the entire operating range. Furthermore, the close agreement between the two models justifies that we do not to include the oleos as part of model (1)–(6) for the bifurcation study of turning solutions.

4 Two-parameter bifurcation study and sensitivity analysis

In this section we present two-parameter bifurcation diagrams, where we track turning solutions in dependence on the steering angle δ and the centre of gravity position CG. By choosing to represent turning solutions in terms of their corresponding forward velocity V_x, we obtain a surface of turning solutions in (δ, V_x, CG)-space. From a practical point of view, this surface is assembled from one-parameter continuation runs in δ, as presented in Section 3, which are computed at discrete values of CG that cover an appropriate range. Two-parameter continuation with AUTO is used to compute the loci of limit point and Hopf bifurcations directly under the variation of both δ and CG. Combining the results from these two computations into a single plot is an effective way of representing the turning dynamics and its stability over the complete range of δ and CG in a single figure. What is more, we are able to perform a sensitivity analysis of turning solutions by computing the respective solution surfaces for different fixed values of other parameters. Specifically, we consider different thrust cases for a heavy aircraft in Section 4.1, and for a light aircraft in Section 4.2. Finally, we show two-dimensional projections of bifurcation curves to highlight certain features that explain qualitative changes in the bifurcation structure when the thrust is changed.

4.1 Heavy aircraft case

Figure 4 shows three surfaces of turning solutions in (δ, V_x, CG)-space for the case of a heavy aircraft. Computed solution branches for fixed discrete values of CG originate on the left side of the diagram; they are initially stable and may become unstable at bifurcation curves on the surface, namely along the curve L of limit point bifurcations and the curve H of Hopf bifurcations. Note that the typical operating range for the centre of gravity position is $CG \in (10\%, 40\%)$. Nevertheless, it is convinient to show an extended CG-range to demonstrate completeness of the overall bifurcation structure.

In Figure 4(a), for a thrust of $T = 16\%$ of maximal thrust, we can see that for a forward CG-position ($CG < 20\%$) the solutions are uniformly stable. At $\delta = 0^\circ$ the aircraft travels in a straight line with $V_x \approx 68$m/s; this initial velocity remains constant under variation of CG. As δ is increased, the velocity of the stable solutions decreases rapidly before starting to plateau out at $\delta \approx 7.5^\circ$; the velocity of solutions continues to decrease gradually down to 0m/s as δ is increased towards 90°. Therefore, for $CG < 20\%$ and with increasing δ, there is a continuous and stable transition from stable large radius solutions via stable small radius solutions all the way to a stationary solution where the nose gear is perpendicular

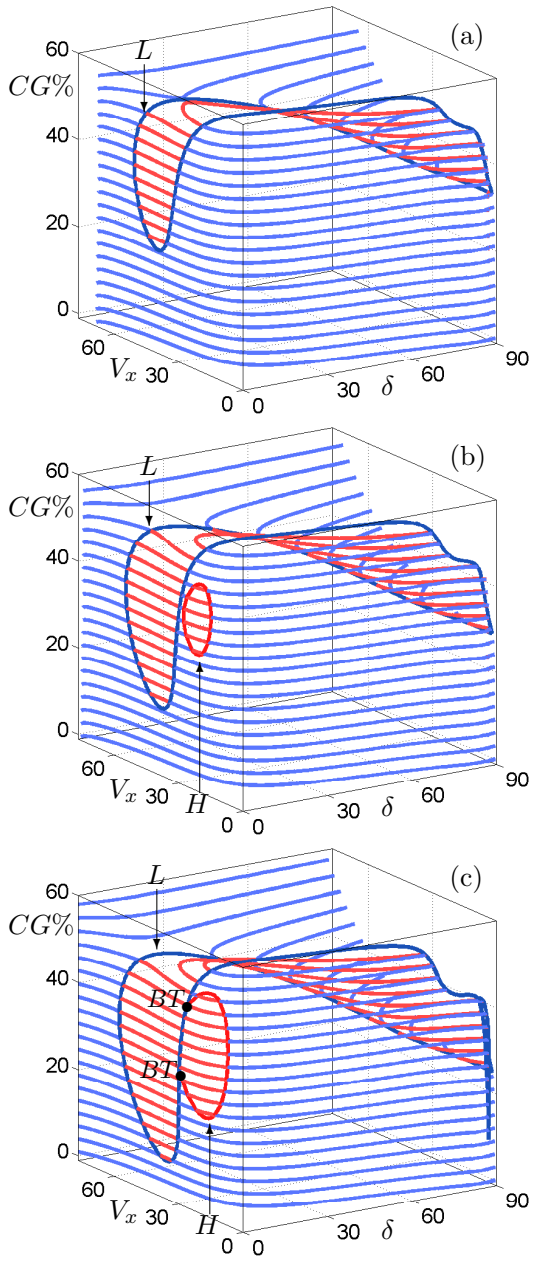

Figure 4: Surfaces of turning solutions in (δ, V_x, CG)-space for a heavy aircraft (as specified in Table 1) and for three fixed values of the thrust; $T = 16\%$ in panel (a), $T = 18\%$ in panel (b), and $T = 20\%$ in panel (c). Stable solutions are blue and unstable solutions are red; limit point bifurcations occur along the thick blue curve L and Hopf bifurcations occur along the thick red curve H; the black dots in panel (c) are points of Bogdanov-Takens bifurcations.

to the direction of motion. For fixed $CG \in (20\%, 50\%)$ the individual solution branches intersect the curve of limit point bifurcations L at two bifurcation points. The minimal point on L at $CG \approx 20\%$ is a cusp point [19] which is discussed further in Section 4.2. When traversing the surface from left to right (fixing CG but varying δ) there are fold points in

the solution branches that occur at intersections with L. When the limit point bifurcation curve L is crossed at the left fold (by increasing δ) the large-radius turning solution becomes unstable and, the aircraft spirals towards and then follows a stable small-radius solution. Similarly, when L is crossed at the right fold (by decreasing δ) the small-radius solution becomes unstable and the aircraft spirals out to and settles down onto a stable large-radius solution. Therefore, as is typical in systems with several limit point bifurcations, there is a hysteresis loop [20] between large- and small-radius turns. A similar hysteresis loop exists between large-radius and small-radius solutions under the variation of CG at fixed values of $\delta > 5°$. At large values of δ and CG the solutions that can be seen in the background of the Figure 4(a) represent large-radius turns for which the nose gear does not generate enough force to keep the aircraft stationary and is, hence, effectively dragged along the ground. For sufficiently large values of $CG > 55\%$ the solution branches become uniformly stable, and they represent large-radius turns only.

When the thrust level T is increased, many of the features of the surface described above persist, but there are some changes. Figure 4(b) shows the surface for $T = 18\%$. Here the forward velocity when $\delta = 0°$ has increased to $V_x \approx 74$m/s. Another change is that the CG-level at which the solution branches first intersect L has decreased to $CG \approx 12\%$. However, the most significant difference is a qualitative change in the dynamics: a closed curve of Hopf bifurcations now bounds a new region of unstable turning solutions on the surface. This new region exists for small δ and $CG \in (30\%, 46\%)$. Crossing H into this region represents a change where the aircraft will attempt to follow a turning circle solution that is unstable (too tight) and, therefore, it loses lateral stability. An example of this type of solution was given in Figure 3(c) and (d); an extensive account of qualitatively different types of laterally unstable solution can be found in Reference [10]. Note further that crossing L at the left fold may now lead to the aircraft moving from a stable large-radius turn to laterally unstable behaviour. However, for $CG < 30\%$ this bifurcation along L does not lead to a loss of lateral stability.

Figure 4(c) shows that there is a further qualitative change when the thrust is increased to $T = 18\%$. Namely, the regions bounded by the curves L and H have increased in size: the minimum point on L occurs now at $CG \approx 5\%$, and H exists over the range $CG \in (20\%, 49\%)$. As a consequence, the regions bounded by the curves L and H have increased in size so much that the curve H is no longer closed but terminates at two intersection points with the curve L. Mathematically, these intersection are known as Bogdanov-Takens bifurcation points [19]. Further details of the topological change associated with the emergence of Bogdanov-Takens bifurcation points are given in Section 4.2. Another change is that the value of CG above which the dynamics are uniformly stable is now reduced, from $CG \approx 55\%$ in Figure 4(a) to $CG \approx 50\%$ in Figure 4(c) .

The properties of the solution surfaces in Figure 4 have physical interpretations in terms of the dynamics of the aircraft. When CG is increased (the CG-position is moved aft) the load on the nose gear is reduced and, thus, the turning force that it can generate is reduced. When making high-velocity turns the aerodynamic forces have a greater effect. In fact, at sufficiently high speeds the holding force generated by the tailplane, which attempts to keep the aircraft traveling in a straight line, becomes more dominant than the turning force generated by the nose gear. This explains that, for a greater value of CG, the left fold of L moves to a larger value of δ because a greater steering angle is required to generate

the necessary turning moment to overcome the aerodynamic holding force. Similarly, the right fold along L is associated with the effect that a decreasing turning moment from the nose gear (as δ is decreased) is being overcome by the aerodynamic forces. Overall, the region bounded by L grows with thrust because at higher velocities the aerodynamic forces are increased. The region H appears and grows with and increasing thrust level because, at higher velocities, the aircraft attempts to make tighter turns to the point where they become laterally unstable.

4.2 Light aircraft case

Figure 5 shows surfaces of turning solutions for the case of a light aircraft for three fixed values of the thrust. They are represented in the same way as for the heavy case, except that the range of CG has been extended to $CG \in (-20\%, 60\%)$. The first result is that the turning behaviour for both loading cases is qualitatively the same in the respective panels for low, medium and high thrust; compare with Figure 4. Nevertheless, there are some quantitative differences that are of importance from the operational point of view. First of all, notice that the thrust levels identified for the light aircraft case are 4% less throughout compared with the heavy case. More specifically, for a value of trust of $T = 12\%$, as shown in Figure 5(a), the initial velocity at $\delta = 0^\circ$ on the individual solution branches is only $V_x \approx 63$m/s. Furthermore, the region bounded by the curve L for small δ does not extend as far into the operational range of CG as for the heavy aircraft case; compare with Figure 4(a). When the thrust is increased by 2% we again find a region of laterally unstable behaviour, bounded by a closed curve of Hopf bifurcations H; see Figure 5(b). However, the size of the instability region bounded by H is dramatically larger when compared to the corresponding heavy aircraft case in Figure 4(b). Namely, the minimal point on L has moved to $CG \approx 15\%$ and the region bounded by H extends over the range $CG \in (1\%, 42\%)$, below the minimal point on L. Therefore, in contrast to the heavy case, passing the bifurcation on the left fold along L always results in the aircraft settling onto laterally unstable behaviour. Furthermore, the region of laterally unstable behaviour in Figure 4(b) is accessible from the left without passing a limit point bifurcation. This means that the region of laterally unstable behaviour could be approached more suddenly at lower velocities. When the thrust in increased further to $T = 16\%$, as is shown in Figure 5(c), the regions bounded by L and H increase further and we again find that H ends at two Bogdanov-Takens points on H. Furthermore, the minimal point on L moves to a negative value of $CG \approx -1\%$ and the range of H extends to $CG \in (-18\%, 48\%)$. Note that a negative value of CG represents a CG-position in front of the leading edge of the mean aerodynamic chord.

Overall, we find in the light aircraft case that the size of the region of laterally unstable behaviour increases much more dramatically when compared with the heavy aircraft case. This is a quantitative observation that is of relevance in spite the fact that the respective panels for the two loading cases are qualitatively the same. Note however that a higher thrust level (of an extra 4% of maximal thrust) is required in the heavy case to achieve similar velocities to the light case. As a result of this the aircraft is much more susceptible to a loss of lateral stability in the light case, as is represented by substantially larger regions of laterally unstable turning solutions.

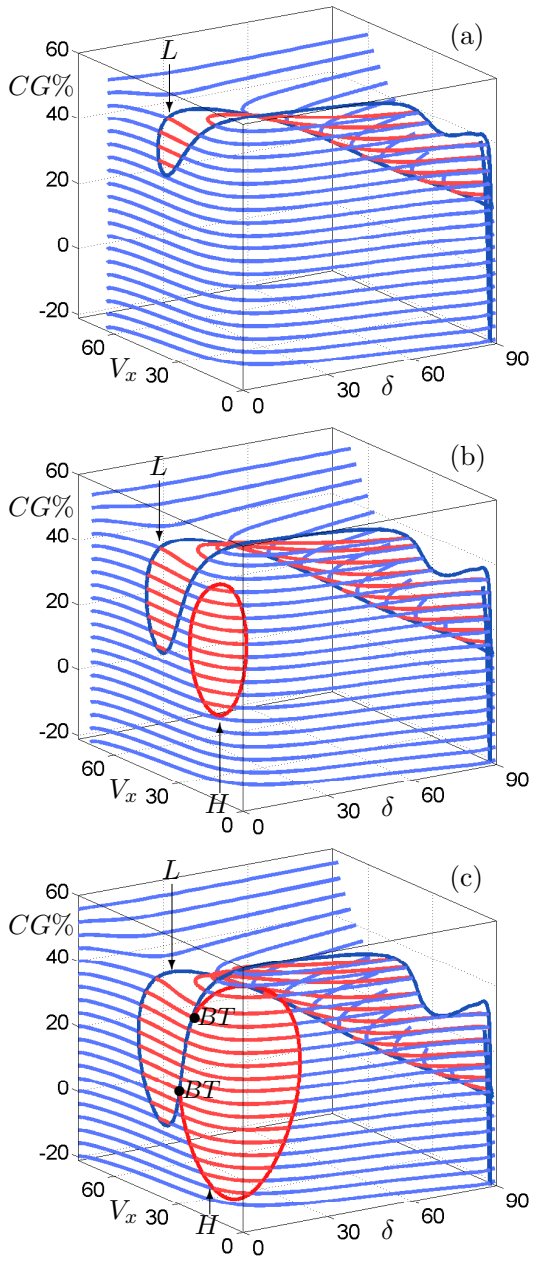

Figure 5: Surfaces of turning solutions in (δ, V_x, CG)-space for a heavy aircraft (as specified in Table 1) and for three fixed values of the thrust; $T = 12\%$ in panel (a), $T = 14\%$ in panel (b), and $T = 16\%$ in panel (c). Stable solutions are blue and unstable solutions are red; limit point bifurcations occur along the thick blue curve L and Hopf bifurcations occur along the thick red curve H; the black dots in panel (c) are points of Bogdanov-Takens bifurcations.

4.3 Qualitative changes of the surfaces of solutions with thrust

The last section demonstrated that the aircraft shows considerable sensitivity to the thrust level: qualitative changes in the overall solution surface occur within a range of 2% of maximum thrust. We now discuss these qualitative changes in more detail. While the

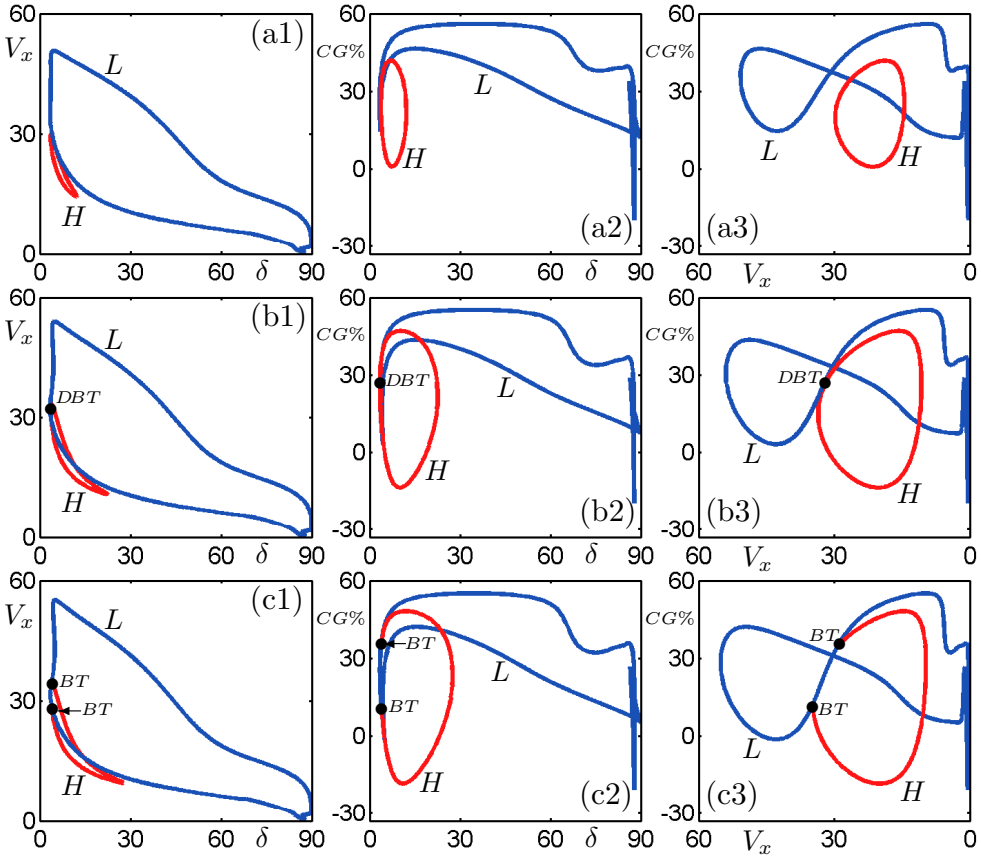

Figure 6: The bifurcation curves L and H for a light aircraft and for thrust levels of $T = 14\%$ in panels (a), $T = 15.4\%$ in panels (b), and $T = 16\%$ in panels (c) are shown in projection onto the (δ, V_x)-plane (first column), onto the (δ, CG)-plane (second column), and onto the (V_x, CG)-plane (third column). Note that the V_x-axis has been reversed in the third column to remain consistent with the surfaces as plotted in Figure 5. The black dots in panels (b) represent degenerate Bogdanov-Takens points and in panels (c) two non-degenerate Bogdanov-Takens points. Compare panels (a) and (c) with Figure 5(b) and (c), respectively.

nature of the transitions is the same for both loading cases, we consider here the case of a light aircraft as presented in Figure 5 because it was seen to be more susceptible to a loss of lateral stability when the thrust is increased.

First of all, the qualitative change between panels (a) and (b) of Figure 5 is due to the fact that a closed curve, or isola, H of Hopf bifurcations appears at a specific thrust value in the interval $T \in (12\%, 14\%)$. Indeed, when the thrust is decreased from $T = 14\%$ then the isola shrinks to a point and disappears. This type of qualitative change of the curve H is due to a smooth transition through a minimum in the associated two-dimensional surface of Hopf bifurcations in (δ, CG, T)-space. This happens at a single value of T in this three-dimensional parameter space, which is why one says that this transition is of codimension-three.

The transition between panels (b) and (c) of Figure 5, on the other hand, is more complicated. As Figure 6 shows by means of projections of the bifurcation curves L and H, it in-

volves the introduction of two Bogdanov-Takens bifurcation points. The mechanism behind this qualitative change is the passage through a codimension-three degenerate Bogdanov-Takens bifurcation, which occurs at an isolated point in (δ, CG, T)-space. Figure 5 shows all three two-dimensional projections of the three-dimensional plots in Figure 5 (b) and (c) and of the intermediate transitional case at $T = 15.4\%$. The (δ, CG)-plane represents the bifurcation diagram in the two parameters, and the same data plotted in the (δ, V_x)-plane and (V_x, CG)-plane reveals the relative positions of the bifurcation curves in terms of the forward velocity V_x. Due to the way the solution surface is located in (δ, V_x, CG)-space, the transition is actually seen most clearly in the third column of Figure 6, which shows the projection onto the (V_x, CG)-plane. Before the degenerate Bogdanov-Takens bifurcation in Figure 6(a) the curve H is indeed closed. At the moment of transition in Figure 6(b) the curve H is still closed, but it now touches the limit point bifurcation curve L at a single point of tangency. At this point there is a degenerate Bogdanov-Takens bifurcation, labelled DBT. Mathematically, this point is characterized by a double zero eigenvalue of the linearization around the respective solution with an additional degeneracy of the higher-order terms of the normal form [19]. After the transition the degenerate Bogdanov-Takens bifurcation point splits up into two non-degenerate Bogdanov-Takens bifurcation points, which are labelled BT in Figure 6(c). These points are of codimension-two, which means that they are isolated points in the two-dimensional (δ, CG)-plane. As a result, the curve H is no longer closed but now ends at the curve L at the two BT points.

Apart from the nature of transitions between qualitatively different bifurcation diagrams of L and H on the solution surface, the projections shown in Figure 6 also reveal quantitative features that are not so evident from the surfaces shown in Figure 5. For example, panels (a1), (b1), and (c1) of Figure 6 shows that there is a region to the left of the bifurcation curves, for $\delta < 3.5°$, where no bifurcations occur. This stable region is independent of both the CG position and the thrust level, so that it might be used to define an upper bound for steering angles used during high velocity turns. A similar bound exists in the heavy case but at a lower value of only $\delta \approx 1.5°$.

5 Conclusions

We presented derivation and implementation details of a fully parametrised mathematical model of a typical mid-sized passenger aircraft. The new model has been validated against an existing industry-tested SimMechanics model that was used in a previous study. Specifically, a comparison between one-parameter bifurcation diagrams of the two models revealed a consistent and accurate agreement over the full range of steering angle for a particular configuration of the aircraft, both for turning solutions as well as a bifurcating branch of periodic solutions (representing unstable turns).

The mathematical model was developed to improve functionality and computational efficiency when used with continuation software. An extensive bifurcation analysis in several operational parameters demonstrated that the new model indeed allows for much more wide-ranging studies of turning as a function of a number of operational parameters. The results of the computations were presented as surfaces of solutions, where the steering angle and the centre of gravity position of the aircraft served as the main parameters. This provides

an effective way of representing the possible dynamics over the complete range of these two parameters in a single figure. Furthermore, it makes it possible to consider sensitivity questions via a study of the influence of other parameters on the solutions surface. As we demonstrated for a heavy and a light aircraft, there are qualitative changes of the solution surface when the thrust level is changed. Corresponding solutions surfaces of the two cases are related qualitatively via a thrust offset of 4% of maximal thrust. Importantly for the practical point of view, the region of laterally unstable solutions was found to increase in size more rapidly with increasing thrust for the light aircraft case.

The mathematical model presented here allows for the systematic investigation of aircraft ground dynamics in dependence on both operational as well as design parameters. Ongoing work focuses on how turning solutions are influenced by tyre properties, taxiway conditions, and the track width of the main landing gears. For example, a preliminary investigation revealed that the dynamics are affected in much the same way when either the thrust is increased or the friction coefficient of the tyres is decreased. Another question under investigation is the study with numerical continuation tools of lateral loading conditions that aircraft experience during ground manoeuvres. Finally, techniques are being developed that allow one to follow specific conditions during a continuation run, such as a fixed radius turn or the detection of the loss of contact between a tyre and the ground.

Acknowledgments

This research is supported by an Engineering and Physical Sciences Research Council (EPSRC) Case Award grant in collaboration with Airbus in the UK.

References

[1] Klyde, D., Myers, T., Magdaleno, R., and Reinsberg, J., 2002, "Identification of the dominant ground handling charactersitics of a navy jet trainer," Journal of Guidance, Control, and Dynamics, **25**(3), pp. 546–552.

[2] Klyde, D., Myers, T., Magdaleno, R., and Reinsberg, J., 2001, "Development and evaluation of aircraft ground handling maneuvers and metrics," AIAA Atmosperic Flight Mechanics Conference, **N/A**(AIAA-2001-4011).

[3] Thompson, J. and Macmillen (Eds.), F., 1998, "Nonlinear flight dynamics of high-performance aircraft," Phil. Trans. R. Soc. Lon. A, **356**(1745).

[4] Khapane, D. P., 2003, "Simulation of asymmetric landing and typical ground maneuvers for large transport aircraft," Aerospace Science and Technology, **7**(8), pp. 611–619.

[5] Doedel, E., Champneys, A., Fairgrieve, T., Kuznetsov, Y., Sandstede, B., and Wang, X., 2001, "Auto 97 : Continuation and bifurcation software for ordinary differential equations," http://indy.cs.concordia.ca/auto/.

[6] Krauskopf, B., Osinga, H. M., and Galán-Vioque, J., 2007, *Numerical Continuation Methods for Dynamical Systems*, Springer.

[7] Venn, D. and Lowenberg, M., 2004, "Non-linear vehicle dynamics using bifurcation methods," Motorsports Engineering Conference and Exhibition.

[8] Charles, G., Lowenberg, M., Stoten, D., Wang, X., and di Bernardo, M., 2002, "Aircraft flight dynamics analysis and controller design using bifurcation tailoring," AIAA Guidance Navigation and Control Conference, **AIAA-2002-4751**.

[9] Bedford, R. and Lowenberg, M., 2004, "Bifurcation analysis of rotorcraft dynamics with an underslung load," AIAA Atmospheric Flight Mechanics Conference, **AIAA-2004-4947**.

[10] Rankin, J., Coetzee, E., Krauskopf, B., and Lowenberg, M., 2008, "Nonlinear ground dynamics of aircraft: Bifurcation analysis of turning solutions," AIAA Modeling and Simulation Technologies Conference, **AIAA-2008-6529**.

[11] Blundell, M. and Harty, D., 2004, *The Multibody Systems Approach to Vehicle Dynamics*, SAE.

[12] Mathworks, 2004, "Model and simulate mechanical systems with simmechanics," http://www.mathworks.com/products/simmechanics/.

[13] Strogatz, S., 2000, *Nonlinear dynamics and chaos*, Springer.

[14] Etkin, B., 1972, *Dynamics of Atmospheric Flight*, Wiley.

[15] Phillips, W., 2004, *Mechanics of Flight*, Wiley.

[16] Jeanneau, M., 2004, "Description of aircraft ground dynamics," Garteur FM AG17 RP0412731, GARTEUR.

[17] Wong, J., 2001, *Theory of Ground Vehicles*, Wiley-Interscience, 3rd ed.

[18] Mitchell, D., 1985, "Calculation of ground performance in take-off and landing," Data Sheet 85029, ESDU.

[19] Kuznetsov, Y., 1998, *Elements of Applied Bifurcation Theory, Applied Mathematical Sciences, Vol. 112*, Springer-Verlag.

[20] Guckenheimer, J. and Holmes, P., 1983, *Nonlinear Oscillations, Dynamical Systems and Bifurcations of Vector Fields, Applied Mathematical Sciences Vol. 42*, Springer.

List of Figure Captions

1. Figure 1: Schematic diagram showing relative positions of force elements F_* acting on the airframe with dimensions defined by l_* in Table 1. Three projections are shown in the aircraft's body coordinate system: the (x, z)-plane in panel (a), the (x, y)-plane in panel (b), and the (y, z)-plane in panel (c). The centre of gravity position is represented by a checkered circle, the aerodynamic centre by a white circle and the thrust centre of each engine by a white square.

2. Figure 2: Lateral force F_y plotted against slip angle α as calculated from Equation (16). The maximum point F_{ymax} that can be generated by the tyre occurs at the 'optimal' slip angle α_{opt}.

3. Figure 3: Comparison between the mathematical model (1)–(6) (black curves) and the SimMechanics model (grey curves). Panel (a) shows one-parameter bifurcation diagrams for varying steering angle δ and fixed $CG = 14\%$ and $T = 19\%$. There is a single branch of turning solutions; stable parts are solid and unstable parts are dashed. Changes in stability occur at the bifurcation points L_{1-4} and H_2. The maximum and minimum forward velocity of a branch of periodic solutions originating at H_2 are also shown. Panel (b) shows the branch of periodic solutions plotted in the (δ, V_y, V_x)-projection; the (grey) surface was computed from the mathematical model and the individual orbits (black closed curves) on the surface were computed with the SimMechanics model. Panel (c) shows a comparison of the individual periodic orbits at $\delta = 10^\circ$ in the (W_z, V_x)-projection. The corresponding CG-trace of the aircraft in the (X, Y) ground plane is shown in panel (d) with markers indicating the orientation of the aircraft at regular time intervals.

4. Figure 4: Surfaces of turning solutions in (δ, V_x, CG)-space for a heavy aircraft (as specified in Table 1) and for three fixed values of the thrust; $T = 16\%$ in panel (a), $T = 18\%$ in panel (b), and $T = 20\%$ in panel (c). Stable solutions are blue and unstable solutions are red; limit point bifurcations occur along the thick blue curve L and Hopf bifurcations occur along the thick red curve H; the black dots in panel (c) are points of Bogdanov-Takens bifurcations.

5. Figure 5: Surfaces of turning solutions in (δ, V_x, CG)-space for a heavy aircraft (as specified in Table 1) and for three fixed values of the thrust; $T = 12\%$ in panel (a), $T = 14\%$ in panel (b), and $T = 16\%$ in panel (c). Stable solutions are blue and unstable solutions are red; limit point bifurcations occur along the thick blue curve L and Hopf bifurcations occur along the thick red curve H; the black dots in panel (c) are points of Bogdanov-Takens bifurcations.

6. Figure 6: The bifurcation curves L and H for a light aircraft and for thrust levels of $T = 14\%$ in panels (a), $T = 15.4\%$ in panels (b), and $T = 16\%$ in panels (c) are shown in projection onto the (δ, V_x)-plane (first column), onto the (δ, CG)-plane (second column), and onto the (V_x, CG)-plane (third column). Note that the V_x-axis has been reversed in the third column to remain consistent with the surfaces as plotted

in Figure 5. The black dots in panels (b) represent degenerate Bogdanov-Takens points and in panels (c) two non-degenerate Bogdanov-Takens points. Compare panels (a) and (c) with Figure 5(b) and (c), respectively.